Journal of
Materials Chemistry A

ROYAL SOCIETY
OF CHEMISTRY

PAPER

View Article Online
View Journal | View Issue

Cite this: *J. Mater. Chem. A*, 2023, **11**, 24890

Received 26th September 2023
Accepted 20th October 2023

DOI: 10.1039/d3ta05836k

rsc.li/materials-a

A PEDOT:PSS nanocomposite film doped with black phosphorus modified with silver nanoparticles for wearable photothermoelectric generators†

Chia-Hao Tsai,[a] Shih-Hung Tung, [b] Jhih-Min Lin[c] and Cheng-Liang Liu *[ad]

Photothermoelectric (PTE) materials have gained significant attention as a promising avenue for converting light into electricity. Herein, the PTE properties of poly(3,4-ethylenedioxythiophene):poly(styrenesulfonate) (PEDOT:PSS) are enhanced by introducing black phosphorus nanosheets (BP NSs) modified with silver nanoparticles (Ag@BP). Under 100 mW cm^{-2} illumination, the resulting PEDOT:PSS/Ag@BP nanocomposite film (P_Ag@BP) exhibits an output voltage of 528.4 μV compared to 300.9 μV for the PEDOT:PSS film. This is attributed to (i) the enhanced photothermal performance of P_Ag@BP, which generates a temperature difference of 18 °C under 100 mW cm^{-2} illumination compared to 10 °C for the PEDOT:PSS film and (ii) the enhanced thermoelectric performance of P_Ag@BP, with an increased power factor of 107.2 μW m^{-1} K^{-2} compared to 32.9 μW m^{-1} K^{-2} for the PEDOT:PSS film. Moreover, a photothermoelectric generator (PTEG) consisting of 36 legs of P_Ag@BP exhibits an open circuit voltage of 16.1 mV, a short circuit current of 47.9 μA, and an output power of 192.6 nW under 120 mW cm^{-2} illumination. Furthermore, when the PTEG is worn on the forearm and exposed to sunlight, it generates an output voltage of 9.2 mV, thus showcasing its potential application in wearable energy harvesting devices.

1. Introduction

Due to the continuing energy crisis and global environmental challenges, there is an increased need to discover effective approaches for meeting the increased demand for sustainable energy solutions.[1–3] Among the various routes investigated, thermoelectric (TE) materials have emerged as a highly promising solution due to their unique capability to directly convert heat into electricity through the Seebeck effect.[4–7] In particular, organic-based materials exhibit inherently low thermal conductivities, making them particularly attractive for TE applications. The energy conversion efficiency of TE materials is generally assessed by using the figure of merit (ZT), which is calculated using the equation $ZT = S^2\sigma T/\kappa$.[8–11] In this equation, S represents the Seebeck coefficient, σ denotes the electrical conductivity, κ signifies the thermal conductivity, and T corresponds to the absolute temperature. To facilitate the characterization of TE properties in organic-based materials, the power factor (PF = σS^2) is commonly used as an evaluation index.[12–25]

Recent studies have focused on an alternative and promising method of energy conversion involving a phenomenon known as the photothermoelectric (PTE) effect. This effect exploits the remarkable ability of certain materials to generate heat (PT) when exposed to light and to convert this heat into electrical energy (TE).[26–35] In some instances, the PTE effect is a synergistic combination of both the PT–TE effect and the photoelectric (PE) effect with the TE effect. The PE–TE effect seamlessly merges the conversion of both light (PE) and heat (TE) into electricity. By harnessing these dual energy sources concurrently, the PE–TE effect holds the potential to substantially boost the overall voltage output of various devices and systems.[36,37] While significant research in this field has focused on inorganic PTE materials, there has been significant attention directed towards organic PTE materials, poly(3,4-ethylenedioxythiophene):poly(styrenesulfonate) (PEDOT:PSS).[36,38–44] These materials offer advantages such as solution processability, flexibility, and low thermal conductivity. However, the presence of PSS in PEDOT leads to the formation of a uniform film, while impeding carrier transport and reducing conductivity.[12,45] This is primarily attributed to the non-conductive nature of PSS, which creates an insulating barrier between the PEDOT grains, thereby hindering carrier mobility within the material. Consequently, post-treatments with substances such as dimethyl sulfoxide (DMSO),[46,47] ethylene glycol (EG),[48] sulfuric

---

[a] *Department of Materials Science and Engineering, National Taiwan University, Taipei 10617, Taiwan. E-mail: liucl@ntu.edu.tw*

[b] *Institute of Polymer Science and Engineering, National Taiwan University, Taipei 10617, Taiwan*

[c] *National Synchrotron Radiation Research Center, Hsinchu 300, Taiwan*

[d] *Advanced Research Center of Green Materials Science and Technology, National Taiwan University, Taipei 10617, Taiwan*

† Electronic supplementary information (ESI) available. See DOI: **https://doi.org/10.1039/d3ta05836k**

acid,[49,50] inorganic salts,[51] and ionic liquids (ILs)[52,53] are crucial for enhancing the TE properties of PEDOT:PSS. Nevertheless, some challenges remain in fully harnessing PEDOT:PSS as a PTE material. For instance, PEDOT:PSS exhibits relatively low light absorption, thereby limiting its performance in photothermal (PT) conversion. In recent years, various strategies have been proposed for improving the PTE properties, and these can be categorized as either heterogeneous or homogeneous synchronous conversion.[40] In heterogeneous asynchronous conversion, an effective PT layer converts light into heat, which is then transferred to a TE layer *via* conduction to generate a temperature difference and produce electricity. For instance, He *et al.* successfully integrated a MoS_2 and polyurethane PT layer with a PEDOT/Te TE film to achieve an enhanced temperature difference of 38 °C and an output power of 0.18 nW under 2625 mW cm^{-2} infrared irradiation,[41] while Xe *et al.* used Au nanoparticles (NPs) as the PT layer coated onto a TE composite layer of PEDOT and Ag_2Se to achieve a 13-fold increase in output power compared to that obtained in the absence of NPs under simulated 100 mW cm^{-2} solar illumination.[42] Meanwhile, homogeneous asynchronous conversion involves the use of a single composite material, often referred to as an "all-in-one" system. This approach minimizes energy loss between interfaces and enhances the PTE effect of the device. For example, Liu *et al.* introduced Te nanowires (NWs) into PEDOT:PSS to obtain a temperature difference of 28 °C and an output power of 0.47 nW under simulated 100 mW cm^{-2} solar illumination,[43] while Tang *et al.* fabricated PEDOT:PSS/IL/SiO_2^+ films to achieve a temperature difference of 46.15 °C and generate an output current and power of approximately 50 μA and 13.57 nW, respectively, under 186.86 mW cm^{-2} IR irradiation.[44]

Due to its desirable characteristics, such as a suitable band gap, high carrier mobility, and efficient PT conversion, black phosphorus (BP) has emerged as a highly promising material with applications in various fields, including photodetectors, sensors, and energy storage.[54–57] In addition, BP has found use in PT therapy due to its significant near-infrared (NIR) extinction coefficient and exceptional PT conversion properties.[58,59] In 2018, Novak *et al.* demonstrated the exceptional TE potential of BP nanosheets (BP NSs) through the development of a PEDOT:PSS/BP NSs nanocomposite film with a superior power factor of 36.2 μW m^{-1} K^{-2} compared to 17.3 μW m^{-1} K^{-2} for PEDOT:PSS.[60] Hence, the synergistic combination of BP with the conductive and TE capabilities of PEDOT:PSS for the optimal conversion of light energy into electrical energy shows great promise for advancements in PTE applications. Moreover, the flexibility exhibited by PEDOT:PSS suggests its suitability for integration into wearable PTE generators (PTEGs).

In the present study, PEDOT:PSS films with outstanding PTE properties are fabricated *via* the incorporation of BP, taking advantage of the homogeneous asynchronous conversion approach. Additionally, the BP is modified with Ag NPs (Ag@BP) to exploit the plasmonic effect arising from the interactions between the incident light and free electrons to generate localized surface plasmons (LSPs).[42] After excitation, the LSPs undergo relaxation *via* two distinct mechanisms, namely radiative decay and non-radiative decay. In radiative decay, the LSPs release their excess energy by re-emitting photons back into free space. In non-radiative decay, however, the energetic charge carriers generated by the relaxing LSPs transfer their energy to the crystal lattice, thus resulting in localized heating.[61] Finally, the films are post-treated with H_2SO_4 to address the reduced conductivity of PEDOT due to encapsulation by the insulating PSS chains in the PEDOT:PSS composite.

The distributions of the BP NSs or Ag@BP within PEDOT:PSS are examined *via* scanning electron microscopy (SEM), while their respective impacts on the phase morphology, conformation, and structure of the PEDOT:PSS nanocomposite films are examined by atomic force microscopy (AFM), X-ray photoelectron spectrometry (XPS), Raman spectroscopy, and grazing-incidence wide-angle X-ray scattering (GIWAXS). Thus, a comprehensive understanding of the interactions and modifications induced by the BP or Ag@BP NSs within the corresponding nanocomposite films is obtained. Finally, the as-fabricated PEDOT:PSS/Ag@BP nanocomposite film (P_Ag@BP) is used to construct a PTEG consisting of 36 legs. This device exhibits an impressive output power of 192.6 nW under 120 mW cm^{-2} irradiation. Furthermore, when the PTEG is attached to the forearm, the PTEG utilizing the temperature difference between the illuminated area of the device and the forearm leads to an output voltage of 9.2 mV. These findings highlight the potential of the P_Ag@BP nanocomposite film in the development of wearable energy harvesting devices that can efficiently generate power from body heat and sunlight.

2. Experimental section

2.1. Materials

Red phosphorus (RP) powder (98%, metals basis), ethylenediamine (ED) (99%), and silver nitrate ($AgNO_3$) (99.9+%, metals basis) were obtained from Alfa Aesar. Poly(3,4-ethylenedioxythiophene) polystyrene sulfonate (PEDOT:PSS, Clevios PH 1000, 1.3 wt%) was purchased from Heraeus. Sulfuric acid (H_2SO_4) (95–98%) was acquired from J. T. Baker. All the solvents and chemicals were used without further purification unless otherwise indicated.

2.2. Synthesis of black phosphorus (BP)

BP powder was synthesized by the wet-chemical method. 1.5 g RP was dispersed in 100 mL ED solvent. Subsequently, the solution was transferred into a Teflon-lined stainless autoclave and subject to heating at 160–180 °C for 12 h.[62] After the solution reached room temperature, it underwent centrifugation at 8000 rpm for 30 min. The precipitate was then rinsed three times with ethanol. Finally, the synthesized BP powder was dried in a vacuum oven at 60 °C overnight. In order to improve the conversion rate of BP, before the wet-chemical method, 1.5 g RP powder was first sealed in two jars under a nitrogen atmosphere. Then, the sealed jars were subject to ball milling at a frequency of 30 Hz for 5 h (Restch MM440).

2.3. Synthesis of BP NSs modified with Ag NPs (Ag@BP)

20 mg of synthesized BP powder was dispersed in 2 mL of ethanol. Following the modified procedure described in

a previous report,[63] 2 mL of $AgNO_3$ (10, 20, 40, 60, and 80 mM) solution was added into 2 mL of obtained BP NSs dispersed solution. The resulting solution was then kept in a dark environment at room temperature for 3, 6, and 12 h. After the reaction, different types of the synthesized Ag@BP nanocomposite were obtained by centrifugation at 8000 rpm for 30 min, followed by rinsing with ethanol three times. Lastly, the synthesized Ag@BP powder was dried in a vacuum oven at 60 °C overnight.

2.4. Fabrication of the PEDOT:PSS nanocomposite

BP powder of 12, 16, 20, 24, and 28 mg was dispersed in 2 mL of ethanol. They were named solutions with concentrations of 0.6, 0.8, 1.0, 1.2, and 1.4 wt%. As for Ag@BP, 16 mg of it was added to 2 mL of ethanol. To prepare the P_BP or P_Ag@BP nanocomposite solution, 0.5 mL of a dispersed solution containing BP NSs (or Ag@BP) was added into 1.5 mL of PEDOT:PSS solution. The resulting mixture was magnetically stirred for 30 min to ensure proper blending and homogeneity before drop-casting. 150 μl of the prepared nanocomposite solution was carefully drop-cast onto a glass substrate (15 × 15 mm), which was cleaned by sonication in acetone, isopropanol, and deionized water for 10 min in each step, followed by oxygen plasma treatment for 10 min. The deposited film was subsequently dried in ambient air at 50 °C for 30 min to remove solvent and annealed at 180 °C for 10 min. Once the annealing step was completed, a post-treatment was performed on the nanocomposite film. Specifically, 200 μl of H_2SO_4 was carefully applied to the nanocomposite film at room temperature for 30 minutes. The nanocomposite film was then rinsed with deionized water and dried at 60 °C to ensure the complete removal of solvent. The same procedure was used to fabricate the PEDOT:PSS film.

2.5. Fabrication of the photothermoelectric generator (PTEG)

In order to construct the generator, a larger substrate with dimensions of 50 × 100 mm was selected. 3.5 mL of the prepared P_Ag@BP nanocomposite solution was carefully drop-cast onto a glass substrate, and the subsequent steps remained the same as those followed for the small-scale sample, with the exception of the post-treatment step. During the post-treatment step, 4.5 mL of H_2SO_4 was carefully applied to the nanocomposite film at room temperature for 30 min and rinsed with deionized water. Notably, when the substrate was immersed in deionized water, the nanocomposite film could detach from the substrate, becoming a free-standing film. Following this, the free-standing film was transferred to a polyethylene terephthalate (PET) sheet, serving as a new flexible substrate. To ensure the complete removal of solvent, the nanocomposite film was then dried at 60 °C. Afterward, the nanocomposite film was cut into rectangular pieces with dimensions of 2.5 × 1 cm. To affix the cut-out film on the non-woven fabric, double-sided tape was utilized. A total of 36 pieces were connected in series using copper wires and silver paste, resulting in the assembly of the generator, as depicted in Fig. 8a and b.

2.6. Measurement

The as-prepared samples described in section 2.4 were cut into rectangular pieces with dimensions of 7 × 15 mm^2, and both ends were coated with silver paste for measurement contact. The TE parameters of polymer nanocomposite films, including Seebeck coefficient and electrical conductivity, were simultaneously measured by using a commercial ZEM-3 measurement system (ADVANCE RIKO Inc., Japan) at 323 K under a helium atmosphere. In the case of PTEG, the temperature gradient was effectively generated by illuminating light emitted from a 300 W Xe lamp (Yamashita Denso YSS-80S, AAA grade) solar simulator. The device allowed for the manipulation of the light intensity to create a varied temperature gradient. To capture and monitor the temperature change of the nanocomposite film, a thermal infrared camera (FLIR A50) was employed. To evaluate the electrical power generation capabilities and obtain the current–voltage (I–V) curves and the power–voltage (P–V) curves of the PTEG, a custom-made measurement system (Keithley 2400 source meter) was utilized under ambient conditions. Furthermore, to determine the light-driven voltage generated by the PTEG, a Keithley 2182A nanovoltmeter was employed. Here, the PTEG was applied to the human forearm for testing. The participant voluntarily participated in this study and signed informed consent before experiments.

3. Results and discussion

3.1. Synthesis and characterization

The transformation of red phosphorus (RP), consisting of P4 tetrahedra, into orthorhombic black phosphorus (BP) with a pleated honeycomb structure *via* the wet-chemical method is demonstrated by the X-ray diffraction (XRD) patterns in Fig. 1a.[62,64] Here, the RP exhibits a characteristic peak at $2\theta = 15.7°$, while the BP exhibits two prominent peaks at $2\theta = 17.6°$ and 27.5° corresponding to the (020) and (021) crystal planes, respectively. As the reaction temperature is increased, the intensity of the characteristic RP peak gradually decreases, while that of BP increases. This observation suggests that higher temperatures enhance the conversion rate of RP to BP. However, the wet-chemical method alone results in the persistence of the RP peak, thus indicating incomplete conversion. To overcome this limitation, a pre-treatment step using the high-energy ball-milling (HEBM) method was introduced prior to the wet-chemical synthesis. This facilitated the transformation of RP to BP, as evidenced by the disappearance of the characteristic RP peak. This is further supported by the Raman spectra in Fig. S1 of the ESI,† where the RP exhibits a distinct, single peak at 349.4 cm^{-1}, while the BP exhibits characteristic peaks at 361.2, 436.0, and 463.7 cm^{-1}, attributed to Ag^1 (out-of-plane mode), B_2g, and Ag^2 (in-plane mode), respectively.[64] Furthermore, the distinctive two-dimensional (2D) nanosheet structure of the BP is revealed by the transmission electron microscope (TEM) image in Fig. 1b, where multiple stacked flakes are observed. Thus, it can be concluded that high-crystallinity BP can be synthesized *via* the combined use of the wet-chemical and HEBM methods.

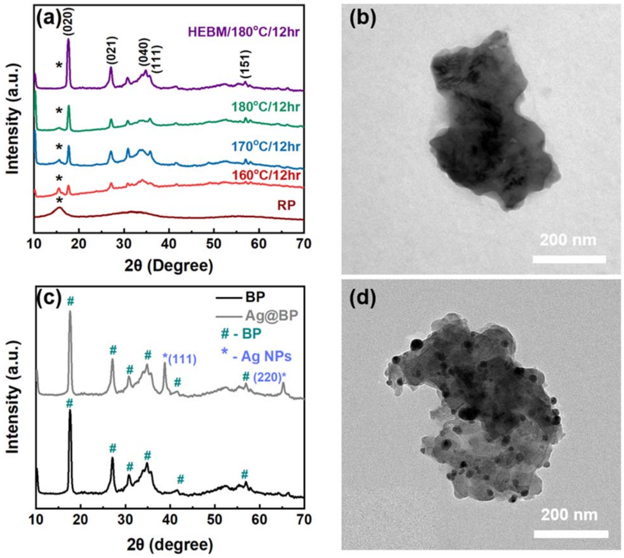

Fig. 1 (a) XRD patterns of RP and BP synthesized under different conditions: 160 °C/12 h, 170 °C/12 h, 180 °C/12 h, and HEBM/180 °C/12 h. (b) TEM image of the as-prepared BP NSs. (c) XRD patterns of the as-prepared BP and Ag@BP. (d) TEM image of Ag@BP.

To enhance the performance of the proposed PTEG device, the BP NSs were modified by introducing Ag NPs on their surfaces to obtain sprinkled structure designated Ag@BP. This is confirmed by the XRD patterns in Fig. 1c, where the introduction of Ag@BP generates two distinct peaks at $2\theta = 38.5°$ and 65.3° due to the respective (111) and (220) crystal planes of the Ag NPs, while the preservation of the BP is demonstrated by the persistence of the characteristic (020) and (021) crystalline peaks at $2\theta = 17.6°$ and 27.5°, respectively. Furthermore, the uniform distribution of the Ag NPs on the surface of BP NSs is clearly revealed by the TEM image in Fig. 1d, where no significant aggregation of the NPs is observed. This confirms the successful synthesis of the homogeneous Ag@BP nanocomposite material and highlights the favourable interactions between the BP and Ag NPs. Furthermore, the results in Fig. S2† indicate the formation of BP NSs with sizes in the range of ~200–300 nm, along with the successful synthesis of the Ag@BP nanocomposites. However, the signals at ~25 nm in Fig. S2b† suggest the possible detachment of some Ag NPs from the surfaces of BP NSs during the dispersion procedure, and this is confirmed by the TEM image in Fig. 1d, which provides visual evidence of the presence of Ag NPs with a size of ~25 nm.

3.2. Thermoelectric properties

The effects of incorporating various amounts of BP NSs on the TE performance of the PEDOT:PSS film are examined in the following section. In addition, the impacts of modifying the BP NSs with various reaction times and concentrations of $AgNO_3$ are investigated. The TE Seebeck coefficients (S_{TE}) of the PEDOT:PSS/BP NSs films (P_BP) are presented in Fig. 2a. Here, the S_{TE} is seen to increase from 14.6 μV K^{-1} for PEDOT:PSS to 21.3, 21.8, 23.8, 24.1, and 24.4 μV K^{-1} at BP NSs concentrations of 0.6, 0.8, 1.0, 1.2, and 1.4 wt%, respectively. This can be primarily attributed to the energy-filtering effect at the interface between the PEDOT:PSS and the BP NSs, as reported in previous studies.[65,66] The presence of BP NSs introduces an energy barrier that effectively blocks low-energy carriers, thus resulting in an increase in the S_{TE} due to the higher average thermal energy of the remaining carriers. This is further supported by the results in Fig. 2d, where the carrier mobility is seen to increase from 0.13 to 0.19 $cm^2 V^{-1} S^{-1}$, and the carrier concentration is seen to decrease from 7.47×10^{22} to 5.75×10^{22} cm^{-3}, upon the addition of 0.8 wt% BP NSs. This phenomenon is entirely consistent with the energy-filtering effect. Here, carriers with low energy are hindered by an energy barrier created by BP NSs. As a result, only carriers with high energy can conquer this barrier, leading to an enhancement in hall mobility while simultaneously reducing the carrier concentration. Meanwhile, the electrical conductivity is seen to increase from 1547.5 S cm^{-1} for the PEDOT:PSS film to 1602.6 S cm^{-1} and 1758.73 S cm^{-1} at BP NSs concentrations of 0.6 and 0.8 wt%, respectively (Fig. 2a). These results demonstrate that the introduction of BP NSs weakens the electron-phonon coupling in the PEDOT:PSS film.[67] Nevertheless, the P_BP with BP NSs concentrations of 1.0, 1.2, and 1.4 wt% exhibits lower electrical conductivities of 1381.5, 1261.1, and 1186.2 S cm^{-1}, respectively. This can be attributed to the high loading levels of BP NSs, which may disrupt the arrangement of the PEDOT:PSS chains, thereby hindering charge-carrier transport.[68] Thus, these results indicate that the optimum concentration of BP NSs is 0.8 wt%. This composition results in a superior TE performance, with a remarkable PF of 83.9 μW m^{-1} K^{-2} (Fig. 2a).

The effects of various reaction times and concentrations of $AgNO_3$ on the synthesis of Ag@BP and its subsequent TE performance are presented in Fig. 2b and c. Specifically, a reaction time of 6 h, combined with a concentration of 40 mM $AgNO_3$, results in the fabrication of a P_Ag@BP nanocomposite film exhibiting significantly improved TE properties. These conditions combine to give a P_Ag@BP film with a superior S_{TE} of 22.83 μV K^{-1}, an electrical conductivity of 2056.6 S cm^{-1}, and a PF of 107.2 μW m^{-1} K^{-2}. This can be attributed to the promotion of charge-carrier transport by the incorporated Ag NPs, along with the enhanced S_{TE} due to the additional energy-filtering effect at the interfaces between the BP NSs and the Ag NPs. This interface effectively increases the carrier mobility from 0.19 $cm^2 V^{-1} S^{-1}$ for the P_BP film to 0.31 $cm^2 V^{-1} S^{-1}$ for the P_Ag@BP film, while reducing the carrier concentration from 5.75×10^{22} to 3.83×10^{22} cm^{-3}, respectively. The presence of Ag NPs creates additional energy barriers, causing a greater hindrance for low-energy carriers. Consequently, this leads to a more increment in mobility and a more decrement in carrier concentration. However, prolonged reaction times of more than 6 h and higher $AgNO_3$ concentrations of more than 40 mM result in inferior TE performance (Fig. 2b and c), in agreement with the above results.

The effects of BP and Ag@BP on the charge-carrier transport are revealed by the temperature-dependent electrical conductivities of PEDOT:PSS, the optimized P_BP film (0.8 wt% BP),

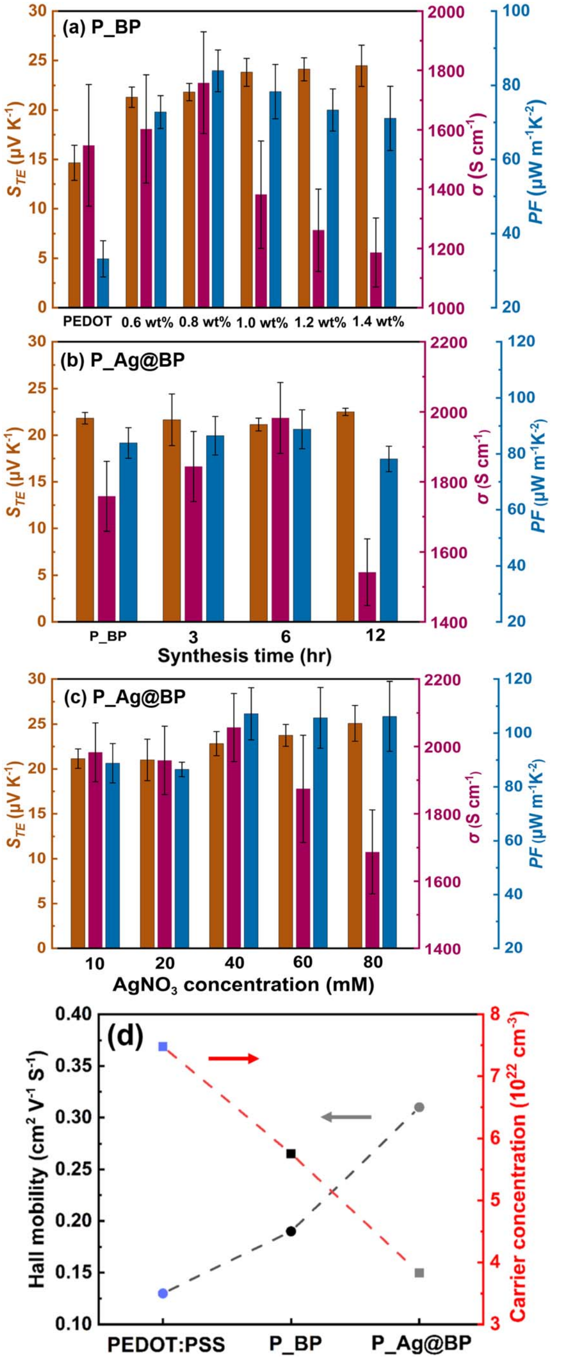

Fig. 2 (a) TE properties of P_BP nanocomposite films with varying BP NSs contents of 0.6, 0.8, 1.0, 1.2, and 1.4 wt%. (b) TE properties of P_Ag@BP nanocomposite films synthesized with different synthesis durations of Ag@BP: 3, 6, and 12 h. (c) TE properties of P_Ag@BP nanocomposite films synthesized with different concentrations of $AgNO_3$ (10, 20, 40, 60, and 80 mM) during Ag@BP synthesis. (d) Mobility and carrier concentration analysis of PEDOT:PSS, P_BP, and P_Ag@BP nanocomposite films.

and the optimized P_Ag@BP film (synthesized using 40 mM $AgNO_3$ for 6 h) in Fig. S3.† Here, all three samples exhibit decreasing electrical conductivity with increasing temperature, thus indicating typically metallic properties. Moreover, Fig. S3† reveals a correlation between the activation energy (E_a) and the energy barrier for charge transport, as described by eqn (1):

$$\sigma = \sigma_{\min} \exp\left(\frac{-E_a}{k_B T}\right) \tag{1}$$

where $\sigma_{\min}$ represents the minimum σ at 363 K and k_B is the Boltzmann constant. Here, the three films were well-fitted with E_a values of 0.0079, 0.0043, and 0.0027 meV for PEDOT:PSS, the optimized P_BP film, and the optimized P_Ag@BP film, respectively. Notably, the E_a value of P_Ag@BP is lower than that of PEDOT:PSS and P_BP, thereby indicating a reduction in the charge-transport barrier. Consequently, the P_Ag@BP film exhibits the highest electrical conductivity among the three films, highlighting the improved charge-carrier transport properties.

3.3. Morphological and microstructural characterization

The morphological and microstructural characteristics of PEDOT:PSS, the optimized P_BP film (0.8 wt% BP), and the optimized P_Ag@BP film (synthesized using 40 mM $AgNO_3$ for 6 h) are revealed by the SEM images and corresponding energy-dispersive X-ray spectroscopy (EDS) results in Fig. 3. Thus, the nanofiber-like structure of PEDOT:PSS is clearly observed in Fig. 3a, and this is retained by P_BP and P_Ag@BP (Fig. 3c and f). Meanwhile, EDS analysis confirms an abundance of sulfur (S) originating from PEDOT:PSS in all three samples (Fig. 3b, d, and g), while phosphorus (P) is well-dispersed within P_BP and P_Ag@BP (Fig. 3e and h). In addition, Fig. 3i reveals the uniform distribution of Ag in P_Ag@BP.

The morphologies of the three nanocomposite films are further revealed by the AFM images in Fig. 4. These results are consistent with the above SEM analysis, thus confirming the presence of the nanofiber-like structure of PEDOT:PSS in the P_BP and P_Ag@BP films. Notably, the introduction of BP or Ag@BP NPs leads to an increased root mean square roughness (R_{rms}) from 2.7 nm for PEDOT:PSS to 4.3 and 4.2 nm for P_BP and P_Ag@BP, respectively. This can be correlated with the presence of white dots in the AFM height images (Fig. 4b and c), which correspond to their respective phase images (Fig. 4e and

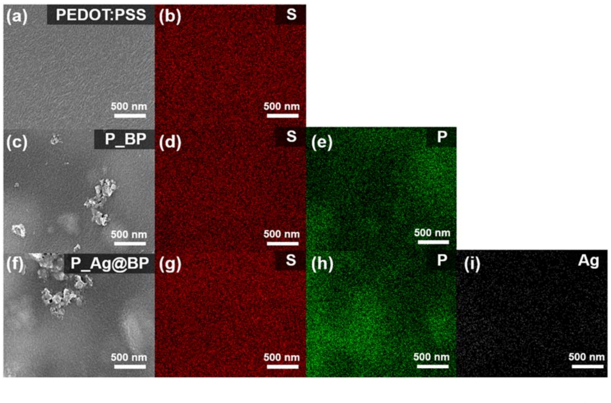

Fig. 3 SEM images and corresponding EDS mapping images of (a and b) the PEDOT:PSS film, (c and e) the P_BP nanocomposite film, and (f–i) the P_Ag@BP nanocomposite film.

f). Thus, the $R_{\rm rms}$ values of the P_BP and P_Ag@BP films increase due to the presence of the BP NSs or Ag@BP.[69,70]

The chemical compositions, molecular structures, and crystallographic characteristics of the PEDOT:PSS, the P_BP, and the P_Ag@BP films are further revealed by the XPS, Raman spectroscopy, and GIWAXS results in Fig. 5. Here, the S 2p XPS peak in the binding energy range of 158–170 eV is deconvoluted into four peaks, corresponding to the S $2p_{3/2}$ and S $2p_{1/2}$ of the sulfonate sulfur in PSS (164–168 eV) and the S $2p_{3/2}$ and S $2p_{1/2}$ of thiophene sulfur in PEDOT (160–164 eV) for all three samples (Fig. 5a–c).[71] Furthermore, the ratio of PSS to PEDOT is calculated from the area ratio of the sulfur peaks, as depicted in Fig. 5d. The results indicate a decrease in the PSS:PEDOT ratio from 1.752 for PEDOT:PSS to 0.895 and 0.877 for P_BP and P_Ag@BP, respectively. This indicates that the introduction of BP NSs or Ag@BP partially weakens the coulombic interactions between the PEDOT and PSS chains, thus leading to the removal of more insulating PSS chains and promoting the connection of PEDOT chains. This contributes to the higher electrical conductivities of the P_BP and P_Ag@BP films.

Meanwhile, the Raman spectra in Fig. S4† reveal a red shift in the $C_\alpha{=}C_\beta$ symmetrical stretching vibration peak of the five-membered rings in the PEDOT chains from 1430.7 cm^{-1} for pristine PEDOT:PSS to 1427.9 cm^{-1} and 1427.0 cm^{-1} for P_BP and P_Ag@BP, respectively. This indicates a transition from the benzenoid to the quinoid structure in the PEDOT chains,[40] thus suggesting that the attachment of smaller PEDOT:PSS segments to larger BP NSs or Ag@BP leads to a weakening of the interactions between PEDOT and PSS, thereby enhancing the dissociation of the PEDOT chains from the PSS upon post-treatment and enabling the transition to the quinoid structure. This is consistent with the abovementioned XPS analysis and provides further evidence for the structural changes induced by the introduction of BP NSs or Ag@BP. In turn, the increased proportion of the quinoid structure and the removal of PSS chains are expected to contribute to the enhanced charge-carrier mobility and electrical conductivity of P_Ag@BP.

The 2D GIWAXS scattering patterns of the various films are presented in Fig. 5e–g, while the corresponding 1D line-cut profiles in the out-of-plane direction are presented in Fig. 5h. The relevant details are summarized in Table 1. Thus, peaks corresponding to the (100) crystal plane of PEDOT are observed at q_z = 0.25, 0.24, and 0.24 Å^{-1} for PEDOT:PSS, P_BP, and P_Ag@BP, respectively, while those due to the (200) crystal plane are observed at q_z = 0.47, 0.46, and 0.46 Å^{-1}, respectively, and those due to the (010) crystal plane are observed at q_z = 1.84, 1.80, and 1.79 Å^{-1}, respectively. These results suggest that the introduction of BP NSs or Ag@BP influences the lamellar spacing and π–π stacking of the PEDOT chains, potentially leading to changes in the crystallinity and molecular ordering within the films. As observed in Fig. 5e–g, it becomes apparent that PEDOT:PSS initially presents a bimodal orientation pattern (edge-on and face-on orientations). However, a noteworthy transformation takes place upon the introduction of BP NSs or Ag@BP. PEDOT:PSS undergoes a distinctive reconfiguration, demonstrating a pronounced preference for the edge-on orientation. Consequently, this transition results in a notable enhancement of its overall degree of orientation. Certainly, the heightened order in the arrangement of P_BP and P_Ag@BP films, which elevates their crystallinity, is substantiated by the emergence of a novel peak aligned with the (300) crystal plane of PEDOT within the 1D line-cut profiles.[72] This is further confirmed by the coherence lengths (L_c) of 4.34, 6.08, and 7.70 Å for PEDOT:PSS, P_BP and P_Ag@BP, respectively. These were calculated from the full width at half maximum (FWHM) values of the (100) PEDOT diffraction peaks by using the Scherrer

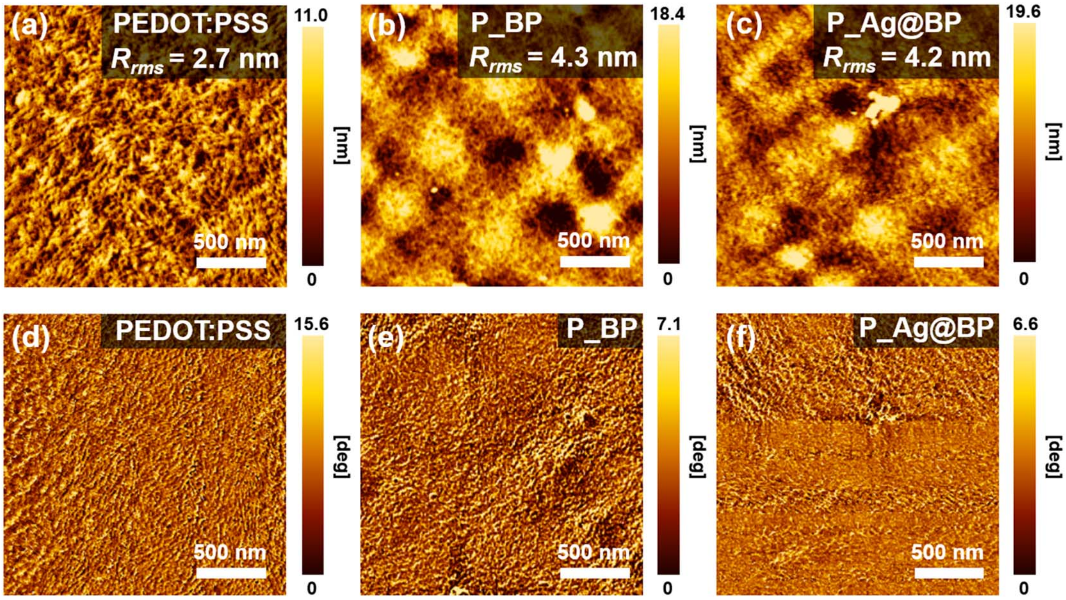

Fig. 4 AFM height images and corresponding phase images of (a and d) the PEDOT:PSS film, (b and e) the P_BP nanocomposite film, and (c and f) the P_Ag@BP nanocomposite film, providing insights into the surface topography and phase characteristics.

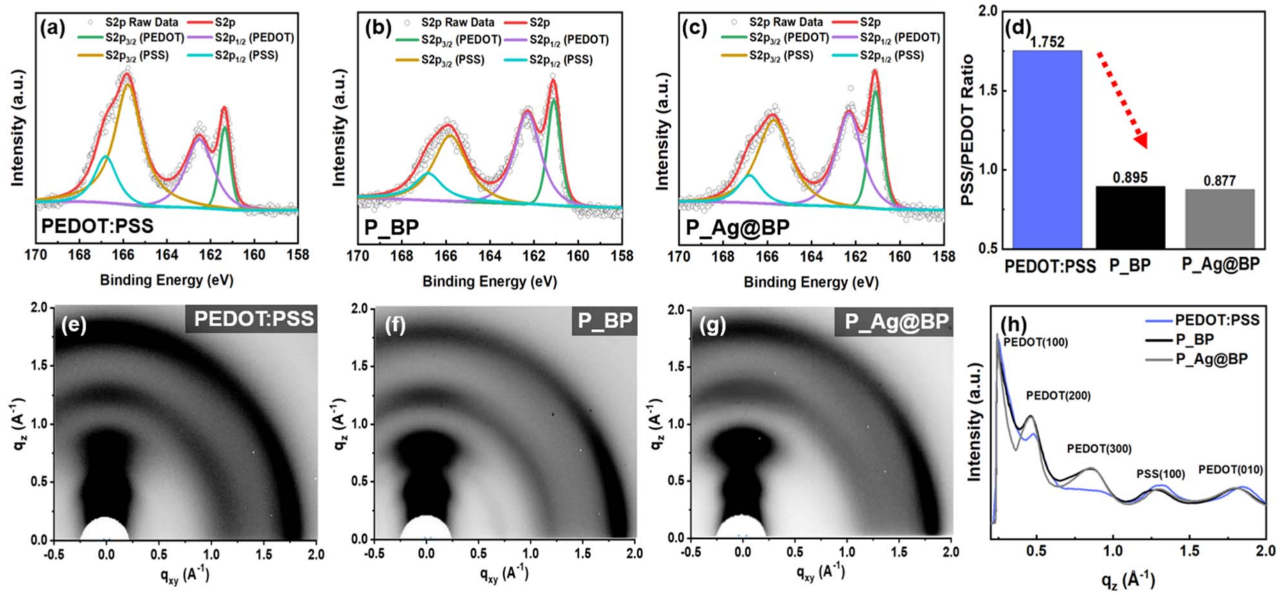

Fig. 5 XPS S 2p spectra of (a) the PEDOT:PSS film, (b) the P_BP nanocomposite film, and (c) the P_Ag@BP nanocomposite film, providing information on the sulfur chemical environment. (d) The ratio of PSS to PEDOT of the three samples is determined by calculating the area ratio of PSS to PEDOT. 2D GIWAXS patterns of (e) the PEDOT:PSS film, (f) the P_BP nanocomposite film, and (g) the P_Ag@BP nanocomposite film. (h) 1D line-cut profile extracted from the GIWAXS pattern of the three samples.

Table 1 Crystallographic parameters of PEDOT for PEDOT:PSS, P_BP, and P_Ag@BP films, as determined by GIWAXS

Sample	(100) Lamellar spacing [Å]	(100) π–π Stacking [Å]	(100) Coherence length [Å]
PEDOT:PSS	25.12	3.40	4.34
P_BP	25.63	3.44	6.08
P_Ag@BP	25.63	3.45	7.70

equation. Thus, P_Ag@BP exhibits the highest crystallinity, followed by P_BP, and then PEDOT:PSS. The above GIWAXS results agree with the Raman spectroscopy and XPS analyses, thus providing a comprehensive understanding of the microstructures and crystalline characteristics of the various nanocomposite films. In brief, the introduction of BP NSs or Ag@BP into PEDOT:PSS preserves the nanofiber-like structure of PEDOT, while effectively weakening the electrostatic forces between the PEDOT and PSS chains. This enables enhanced connections among the PEDOT chains, thus resulting in the formation of larger PEDOT domains and a higher proportion of the quinoid structure, thereby improving the charge-carrier mobility and conductivity of the modified films. Notably, P_Ag@BP demonstrates the most extensive removal of PSS chains, leading to the formation of the largest PEDOT crystalline domains and the highest proportion of the quinoid structure, ultimately providing the highest electrical conductivity.

3.4. Photothermoelectric properties

The PTE properties of the various films, in terms of their ability to convert light efficiently into useable energy, were comprehensively assessed by using an infrared (IR) camera and a lab-built experimental setup to monitor the temperature variations while simultaneously illuminating the film with a solar simulator. The IR images of the PEDOT:PSS, the P_BP, and the P_Ag@BP films captured at various irradiation times under a light intensity of 100 mW cm^{-2} are presented in Fig. 6a, while the corresponding time-dependent temperatures of the films are presented in Fig. 6b. Here, it is evident that the PEDOT:PSS film exhibits a relatively poor PT conversion, consistently displaying the lowest temperature rise throughout the irradiation process. The maximum temperature reached by the PEDOT:PSS film is approximately 42.0 °C, compared to maximum temperatures of 47.3 and 50.1 °C for the P_BP and P_Ag@BP films, respectively. This can be attributed to the superior absorption capabilities of the P_BP and P_Ag@BP films, as confirmed by the UV-vis-NIR spectra in Fig. S5,† where the P_BP and P_Ag@BP films exhibit stronger absorption than does the PEDOT:PSS film, especially in the near-infrared (NIR) range between 800 and 1000 nm. This, in turn, is attributed to the incorporation of the BP NSs, which improve the light absorption and possess impressive PT conversion capabilities. Consequently, P_BP and P_Ag@BP can attain higher temperatures than PEDOT:PSS when exposed to light. Moreover, P_Ag@BP demonstrates the most outstanding light absorption properties and generates the highest temperature after illumination, which can be primarily attributed to the plasmonic effect induced by the presence of Ag NPs. Thus, the introduction of Ag NPs results in a significant enhancement in the electric field through light scattering, thereby increasing the light absorption efficiency.[73]

Consequently, the improved absorption capabilities directly contribute to the overall enhancement of PT conversion properties. To further investigate the PT properties, additional IR

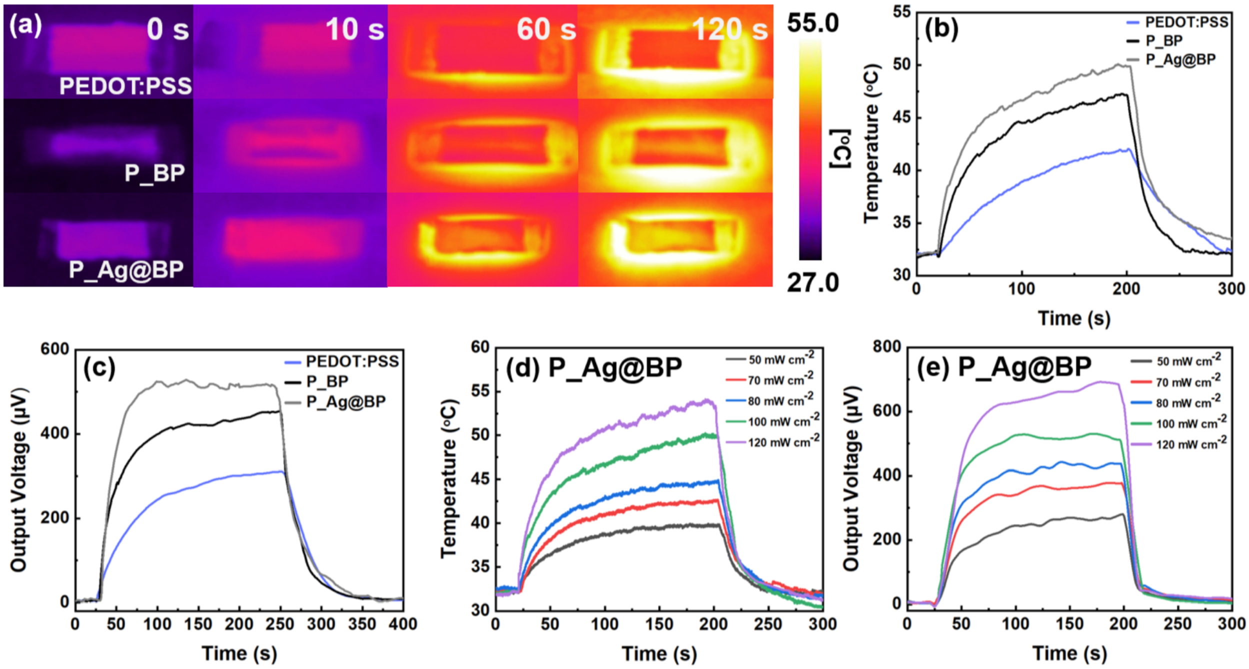

Fig. 6 (a) IR images of PEDOT:PSS, P_BP, and P_Ag@BP at different exposure times, (b) time-dependent temperature for PEDOT:PSS, P_BP, and P_Ag@BP, and (c) time-dependent output voltage for PEDOT:PSS, P_BP, and P_Ag@BP under illumination with an intensity of 100 mW cm^{-2}. (d) Time-dependent temperature and (e) output voltage for P_Ag@BP were recorded under different light intensities of 50, 70, 80, 100, and 120 mW cm^{-2}.

images are captured at different irradiation times under varying light intensities for PEDOT:PSS, P_BP, and P_Ag@BP (Fig. S6–S8†). The results derived from these images are summarized and presented in Fig. 6d and S9,† which depict the time-dependent temperature under different light intensities. Here, the temperature of each film is seen to increase as the light intensity increases, with that of P_Ag@BP exhibiting the greatest increase under all illumination conditions.

The initial step in the PTE effect of the device involves the conversion of incident light into thermal energy. This creates a temperature difference between the illuminated (hot) side and the unilluminated (cold) side, which leads to the generation of electricity *via* the PTE effect. To investigate this effect in the individual films, half of each film was covered with aluminum foil to prevent direct light irradiation and the covered portion was defined as the cold side. The results in Fig. 6c indicate maximum output voltages of 300.9, 435.5, and 528.4 μV for the PEDOT:PSS, the P_BP, and the P_Ag@BP films, respectively. Moreover, the response times (*i.e.*, the time taken to attain 90% of the maximum output voltage) of the PEDOT:PSS, P_BP, and P_Ag@BP films are 100, 60, and 40 s, respectively. The increased output voltages and photosensitivities of P_BP and P_Ag@BP are ascribed to the incorporation of the BP NSs, which exert a dual effect by augmenting the TE properties and magnifying the PT performance *via* their remarkable PT conversion capabilities. Moreover, P_Ag@BP exhibits the greatest photosensitivity and fastest response due to the plasmonic effects of the Ag NPs. Thus, when the material is exposed to light, the presence of Ag NPs leads to a localized enhancement in the electric field, which not only facilitates better absorption of photons, thereby improving the light absorption capability, but also increases the overall photosensitivity of the material.[74] Additionally, the response time is intricately linked to the PTE conversion, with the shorter response time indicating a higher performance. Therefore, the presence of Ag NPs not only enhances the TE and PT effects but also leads to an overall improvement in the PTE performance. Similar trends to those in the PT effect are observed in Fig. 6e and S10,† where the output voltage of each film is seen to increase with the increase in light intensity. Moreover, from the slope of the output voltage *vs.* light intensity (Fig. S11†), the ability of the device to generate voltage per unit of light intensity is calculated to be 2.8, 4.3, and 5.3 μV cm^2 mW^{-1} for the PEDOT:PSS, P_BP, and P_Ag@BP films, respectively. This further demonstrates the potential application of the P_Ag@BP film as a high-performance PTE device.

Furthermore, the output voltage of each film is plotted against the temperature difference induced by irradiation at various light intensities in Fig. 7a–c, from which the PTE Seebeck coefficient (S_{PTE}) is calculated to be 16.1, 28.7, and 30.5 μV K^{-1} for PEDOT:PSS, P_BP, and P_Ag@BP, respectively. Notably, the S_{PTE} of the PEDOT:PSS film closely resembles its S_{TE} (14.6 μV K^{-1}), whereas the S_{PTE} values of the P_BP and P_Ag@BP films surpass their respective S_{TE} values of 21.8 and 22.8 μV K^{-1}, respectively (Fig. 7d). This can be attributed to the generation of a photo-induced voltage when the entire film is under illumination (thus leaving no temperature gradient for TE conversion), as demonstrated in Fig. S12.† In this case, the voltage generated under illumination is predominantly photo-induced.

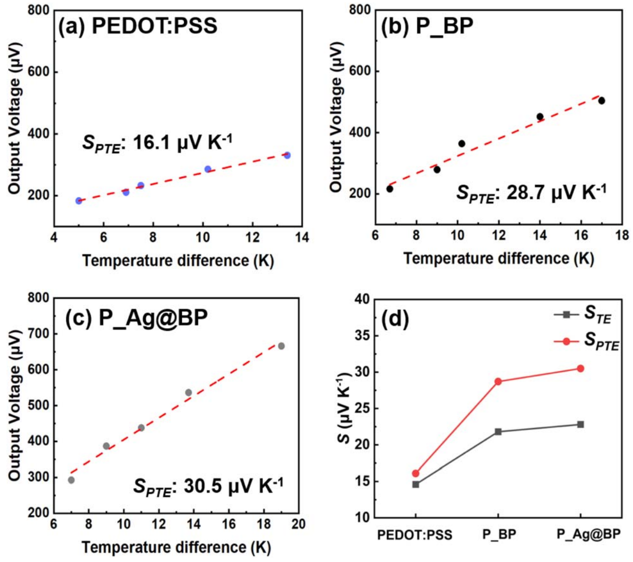

Fig. 7 A linear relationship between the output voltage and temperature difference for (a) PEDOT:PSS, (b) P_BP, and (c) P_Ag@BP samples, used for calculating S_{PTE}. (d) Comparison of S_{TE} and S_{PTE} for PEDOT:PSS, P_BP, and P_Ag@BP.

The photo-induced voltage arises from the movement of photogenerated nonequilibrium carriers, which encompass both electrons and holes. Specifically, there is an additional generation of nonequilibrium electrons and holes due to the separation of excitons between the donor material (PEDOT:PSS) and the acceptor material (BP NSs or Ag@BP) at the illuminated end of the device. This separation process results in the migration of these extra nonequilibrium electrons and holes from the illuminated end to the dark end. Analyzing the outcomes in Fig. S12,† it becomes evident that all devices yield a positive output voltage. Hence, we can deduce that the mobility of nonequilibrium holes exceeds that of nonequilibrium electrons. When combined with the thermoelectric (TE) effect, this difference in mobility significantly boosts the output voltage. In essence, the incorporation of BP NSs or Ag@BP not only amplifies the photothermoelectric (PTE) effect but also introduces the photoelectric (PE) effect.[37] Moreover, upon modification of the BP NSs with Ag NPs, the resulting P_Ag@BP film exhibits a slight enhancement in the photoelectric effect compared to that of the P_BP film. Consequently, the P_Ag@BP film provides the optimal performance in terms of the PTE effect.

Based on the excellent PTE properties of the P_Ag@BP film, it is deemed highly suitable for application in a PTEG device. Hence, such a device was constructed using 36 head-to-tail connected legs consisting of the P_Ag@BP film, as detailed in the Experimental section and depicted in Fig. 8a and b. The results in Fig. S13† indicate that the output voltage of the PTEG increases proportionally with the increase in light intensity, reaching a maximum output of 16.5 mV at 120 mW cm^{-2}

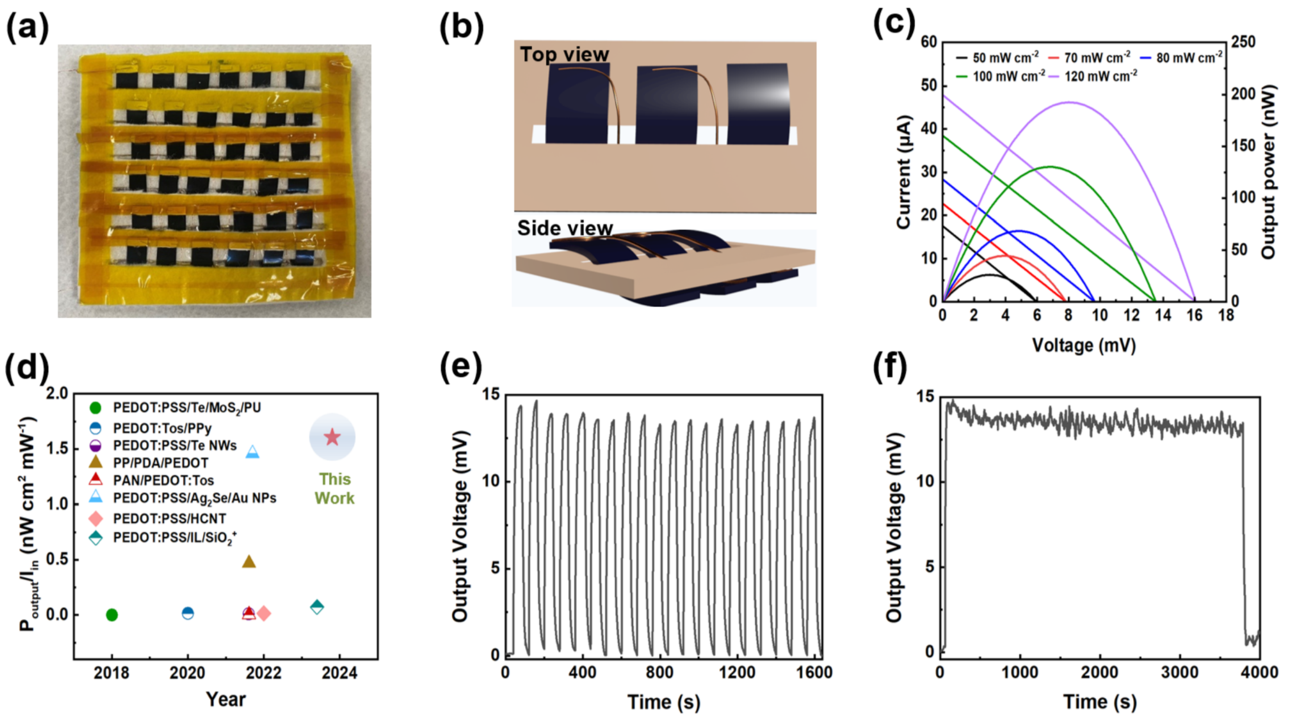

Fig. 8 (a) Photograph of the PTEG showcasing its construction with 36 head-to-tail connection legs. (b) Schematic diagram depicting the side view and the top view of the structure of the PTEG, (c) Current and output power plotted against voltage for the PTEG under different light intensities of 50, 70, 80, 100, and 120 mW cm^{-2}. (d) Comparison of the device's ability to generate voltage per unit of light intensity for PTEGs in previous and this work. (e) Cycling test results demonstrating the stability of the PTEG and (f) long-term stability test of output voltage for the PTEG under 100 mW cm^{-2} illumination.

illumination. This is because the higher light intensity generates a greater temperature difference. Furthermore, the plots of current (left-hand axis) and the output power (right-hand axis) against voltage under various light intensities in Fig. 8c indicate that the PTEG exhibits an open circuit voltage of 16.1 mV, a short circuit current of 47.9 μA, and an output power of 192.6 nW at a light intensity of 120 mW cm^{-2}. Moreover, the performance of the as-fabricated PTEG is seen to be highly competitive when compared with previously reported devices in Fig. 8d.[40–44,75–77] We utilize units that involve dividing output power (nW) by light intensity (mW cm^{-2}), allowing us to evaluate and compare our study with other references in relation to energy generation per unit of light intensity. Our results illustrate that our device attains the highest power output for a given light intensity. The stability of the as-fabricated PTEG is demonstrated in Fig. 8e, where the light-driven voltage remains stable during 20 cycles of light on/off switching at 100 mW cm^{-2} illumination. Additionally, the results in Fig. 8f demonstrate that the PTEG maintains a stable output voltage for 1 h under the same illumination. These findings further demonstrate the potential practicality of the PTEG prototype in real-world applications.

Finally, the practical application of the as-fabricated PTEG as a wearable device attached to the forearm for the utilization of waste heat from daily life is demonstrated in Fig. 9. For example, when the wearer is indoors, the forearm temperature is higher than the surface temperature of the PTEG device, thus making the forearm the heat source. Therefore, the portion of the film in direct contact with the forearm is considered the hot side, while the upper surface of the film represents the cold side. The IR image in Fig. 9a shows a forearm temperature of 33.1 °C and a device surface temperature of 27.8 °C, thus indicating a temperature difference of approximately 5.3 °C. This enables the wearable device to generate an output voltage of 5.4 mV. Conversely, when the wearer is outdoors, the PTEG is exposed to sunlight as the heat source, so that the upper surface of the film functions as the hot side, while the lower surface in direct contact with the forearm becomes the cold side. Thus, the IR thermometer indicates a temperature of 40.5 °C for the upper surface of the film, while the forearm temperature is 31.9 °C, giving a temperature difference of approximately 8.6 °C (Fig. 9b). As a result, the wearable PTE device is able to generate an output voltage of 9.2 mV. These results highlight the remarkable potential of the wearable PTE device to generate electricity in various circumstances, whether indoors or outdoors, on sunny or cloudy days. The ability to create a slight temperature difference on the device can be harnessed to produce electricity. Therefore, the development of wearable devices with excellent stability and high performance becomes imperative. By utilizing these innovative wearable devices, it is possible to collect and repurpose the abundant waste heat generated in our daily routines, thereby contributing to energy harvesting and sustainability efforts.

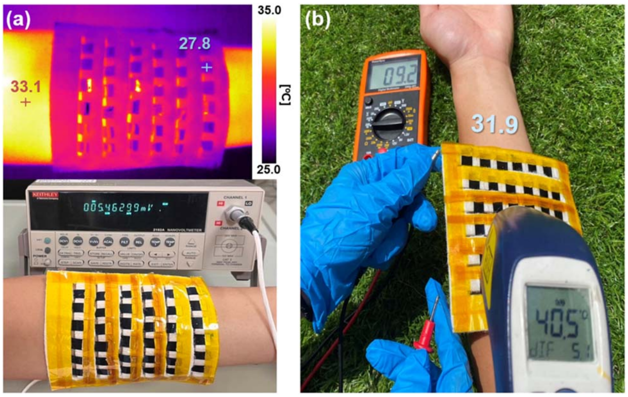

Fig. 9 (a) The IR image and corresponding output voltage measurements of the PTEG worn on the forearm were captured indoors. (b) Output voltage and the temperatures of the PTEG (40.5 °C) and the forearm (31.9 °C) were recorded when the PTEG was worn on the forearm exposed to sunlight.

4. Conclusion

In conclusion, the present study successfully demonstrated highly efficient PTE materials based on PEDOT:PSS modified with crystalline BP NSs. Furthermore, the BP NSs were uniformly decorated with Ag NPs. The TE performances of various concentrations of BP NSs in the PEDOT:PSS matrix were investigated to find that 0.8 wt% provides the optimum performance, with a PF of 83.9 μW m^{-1} K^{-2}. In addition, the effects of various reaction times and $AgNO_3$ concentrations on the Ag@BP nanocomposites were explored, indicating an optimum reaction time of 6 h and an optimum $AgNO_3$ concentration of 40 mM. Under these conditions, the P_Ag@BP film exhibited an S_{TE} of 22.83 μV K^{-1}, an electrical conductivity of 2056.6 S cm^{-1}, and a PF of 107.2 μW m^{-1} K^{-2}. The observed increase in S_{TE} was attributed to the energy-filtering effect, which facilitates the transport of carriers with higher thermal energy. Furthermore, the enhanced electrical conductivity was ascribed to the modification of the electron–phonon coupling effect and the conformational change of PEDOT from a benzenoid to a quinoid structure, thus resulting in larger PEDOT domains. Moreover, the P_Ag@BP film exhibited excellent PT conversion properties, with a maximum temperature of 50.1 °C under 100 mW cm^{-2} irradiation, compared to 42.0 and 47.3 °C for PEDOT:PSS and P_BP, respectively. When integrated into a PTEG device and subjected to 120 mW cm^{-2} illumination, P_Ag@BP generated an output voltage of 16.5 mV, a current of 47.9 μA, and an output power of 192 nW. These findings open up possibilities for the utilization of P_Ag@BP in the development of efficient and sustainable wearable PTE devices, thus contributing to the advancement of green energy generation.

Conflicts of interest

There are no conflicts to declare.

Acknowledgements

The authors acknowledge the financial support from the 2030 Cross-Generation Young Scholars Program by the National

Science and Technology Council (NSTC) in Taiwan, under grants 111-2628-E-002-014 and 112-2628-E-002-013, and Advanced Research Center for Green Materials Science and Technology from The Featured Area Research Center Program within the framework of the Higher Education Sprout Project by the Ministry of Education (112L9006). The authors also thank Beamlines TLS 13A/17A and TPS 25A at the National Synchrotron Radiation Research Center (NSRRC) of Taiwan for providing beamtime. The authors thanks Ms S.-J. Ji and Ms C.-Y. Chien of National Taiwan University for their assistance in SEM/TEM experiments.

References

1 Y. Wang, R. Zou, F. Liu, L. Zhang and Q. Liu, *Appl. Energy*, 2021, **304**, 117766.

2 G. Wu, R. Liang, M. Ge, G. Sun, Y. Zhang and G. Xing, *Adv. Mater.*, 2022, **34**, 2105635.

3 Z. Liu, B. Tian, Y. Li, Z. Guo, Z. Zhang, Z. Luo, L. Zhao, Q. Lin, C. Lee and Z. Jiang, *Small*, 2023, 2304599.

4 I. Petsagkourakis, N. Kim, K. Tybrandt, I. Zozoulenko and X. Crispin, *Adv. Electron. Mater.*, 2019, **5**, 1800918.

5 B. Huo and C. Y. Guo, *Molecules*, 2022, **27**, 6932.

6 Y. Zhang, W. Wang, F. Zhang, K. Dai, C. Li, Y. Fan, G. Chen and Q. Zheng, *Small*, 2022, **18**, 2104922.

7 T. Cao, X.-L. Shi and Z.-G. Chen, *Prog. Mater. Sci.*, 2023, **131**, 101003.

8 D. Bao, J. Chen, Y. Yu, W. Liu, L. Huang, G. Han, J. Tang, D. Zhou, L. Yang and Z.-G. Chen, *Chem. Eng. J.*, 2020, **388**, 124295.

9 X. L. Shi, J. Zou and Z. G. Chen, *Chem. Rev.*, 2020, **120**, 7399.

10 L. Deng, Y. Liu, Y. Zhang, S. Wang and P. Gao, *Adv. Funct. Mater.*, 2022, **33**, 2210770.

11 W. Li, Y. Luo, T. Xu, Z. Ma, C. Li, Y. Wei, Y. Tao, Y. Qian, X. Li, Q. Jiang and J. Yang, *Small*, 2023, **19**, 2301963.

12 Z. Fan and J. Ouyang, *Adv. Electron. Mater.*, 2019, **5**, 1800769.

13 N. Nandihalli, C.-J. Liu and T. Mori, *Nano Energy*, 2020, **78**, 105186.

14 F. Zhang and C.-a. Di, *Chem. Mater.*, 2020, **32**, 2688.

15 T. L. D. Tam and J. Xu, *J. Mater. Chem. A*, 2021, **9**, 5149.

16 S. Xu, X.-L. Shi, M. Dargusch, C. Di, J. Zou and Z.-G. Chen, *Prog. Mater. Sci.*, 2021, **121**, 100840.

17 L. Zhang, X.-L. Shi, Y.-L. Yang and Z.-G. Chen, *Mater. Today*, 2021, **46**, 62.

18 J. Tang, Y.-H. Pai and Z. Liang, *ACS Energy Lett.*, 2022, **7**, 4299.

19 A. Tripathi, Y. Lee, S. Lee and H. Y. Woo, *J. Mater. Chem. C*, 2022, **10**, 6114.

20 D. Zhou, H. Zhang, H. Zheng, Z. Xu, H. Xu, H. Guo, P. Li, Y. Tong, B. Hu and L. Chen, *Small*, 2022, **18**, 2200679.

21 H. Song, Q. Meng, Y. Lu and K. Cai, *Adv. Electron. Mater.*, 2019, **5**, 1800822.

22 Y. Yang, H. Deng and Q. Fu, *Mater. Chem. Front.*, 2020, **4**, 3130.

23 Y. Hao, X. He, L. Wang, X. Qin, G. Chen and J. Yu, *Adv. Funct. Mater.*, 2021, **32**, 2109790.

24 Y. Jia, Q. Jiang, H. Sun, P. Liu, D. Hu, Y. Pei, W. Liu, X. Crispin, S. Fabiano, Y. Ma and Y. Cao, *Adv. Mater.*, 2021, **33**, 2102990.

25 M. Li, Y. Xiong, H. Wei, F. Yao, Y. Han, Y. Du and D. Xu, *Nanoscale*, 2023, **15**, 11237.

26 W. Zhou, Q. Fan, Q. Zhang, L. Cai, K. Li, X. Gu, F. Yang, N. Zhang, Y. Wang, H. Liu, W. Zhou and S. Xie, *Nat. Commun.*, 2017, **8**, 14886.

27 Y. Zhong, L. Zhang, V. Linseis, B. Qin, W. Chen, L.-D. Zhao and H. Zhu, *Nano Energy*, 2020, **72**, 104742.

28 G. Li, S. Yin, C. Tan, L. Chen, M. Yu, L. Li and F. Yan, *Adv. Funct. Mater.*, 2021, **31**, 2104787.

29 P. Zhou, J. Lin, W. Zhang, Z. Luo and L. Chen, *Nano Res.*, 2021, **15**, 5376.

30 R. Li, M. Wu, S. Aleid, C. Zhang, W. Wang and P. Wang, *Cell Rep. Phys. Sci.*, 2022, **3**, 100781.

31 B. Lv, Y. Liu, W. Wu, Y. Xie, J. L. Zhu, Y. Cao, W. Ma, N. Yang, W. Chu, Y. Jia, J. Wei and J. L. Sun, *Nat. Commun.*, 2022, **13**, 1835.

32 Y. Wu, Y. Li, Y. Long, Y. Xu, J. Yang, H. Zhu, T. Liu and G. Shi, *ACS Appl. Mater. Interfaces*, 2022, **14**, 40437.

33 Z. Liu, Z. Wu, S. Zhang, Y. Lv, E. Mu, R. Liu, D. Zhang, Z. Li, S. Li, K. Xu and Z. Hu, *Sci. Adv.*, 2022, **8**, 7500.

34 X. Li, M. Sheng, J. Liang, J. Zheng, Y. Zheng, S. Wang, Q. Li, L. D. Zhao, Y. Deng and Y. Wang, *Adv. Funct. Mater.*, 2023, **33**, 2303352.

35 J. Wang, Z. Xie, J. A. Liu, G. Lu, R. Zhou and J. T. W. Yeow, *Adv. Mater. Technol.*, 2023, **8**, 2300309.

36 X. Lan, Y. Liu, J. Xu, C. Liu, P. Liu, C. Liu, W. Zhou and F. Jiang, *Nanoscale*, 2022, **14**, 18003.

37 G. Li, Y. Hu, J. Chen, L. Liang, Z. Liu, J. Fu, C. Du and G. Chen, *Adv. Funct. Mater.*, 2023, **33**, 2303861.

38 S. Yue, H. Cheng, H. He, X. Guan, Q. Le, X. Shu, S. Shi, J. Chen and J. Ouyang, *J. Mater. Chem. A*, 2021, **9**, 16725.

39 J. Wang, Z. Xie, G. Lu, J. A. Liu and J. T. W. Yeow, *Microsyst. Nanoeng.*, 2023, **9**, 21.

40 X. Z. Jin, H. Li, Y. Wang, Z. Y. Yang, X. D. Qi, J. H. Yang and Y. Wang, *ACS Appl. Mater. Interfaces*, 2022, **14**, 27083.

41 M. He, Y.-J. Lin, C.-M. Chiu, W. Yang, B. Zhang, D. Yun, Y. Xie and Z.-H. Lin, *Nano Energy*, 2018, **49**, 588.

42 C. Xin, Z. Hu, Z. Fang, M. Chaudhary, H. Xiang, X. Xu, L. Aigouy and Z. Chen, *Mater. Today Energy*, 2021, **22**, 100859.

43 Y. Liu, X. Lan, J. Xu, W. Zhou, C. Liu, C. Liu, P. Liu, M. Li and F. Jiang, *ACS Appl. Mater. Interfaces*, 2021, **13**, 43155.

44 X. H. Tang, X. Z. Jin, Q. Zhang, Q. Zhao, Z. Y. Yang and Q. Fu, *ACS Appl. Mater. Interfaces*, 2023, **15**, 23286.

45 H. He and J. Ouyang, *Acc. Mater. Res.*, 2020, **1**, 146.

46 C. Liu, B. Lu, J. Yan, J. Xu, R. Yue, Z. Zhu, S. Zhou, X. Hu, Z. Zhang and P. Chen, *Synth. Met.*, 2010, **160**, 2481.

47 G. H. Kim, L. Shao, K. Zhang and K. P. Pipe, *Nat. Mater.*, 2013, **12**, 719.

48 S. Liu, H. Deng, Y. Zhao, S. Ren and Q. Fu, *RSC Adv.*, 2015, **5**, 1910.

49 J. Kim, J. G. Jang, J.-I. Hong, S. H. Kim and J. Kwak, *J. Mater. Sci.: Mater. Electron.*, 2016, **27**, 6122.

50 S. Xu, M. Hong, X.-L. Shi, Y. Wang, L. Ge, Y. Bai, L. Wang, M. Dargusch, J. Zou and Z.-G. Chen, *Chem. Mater.*, 2019, **31**, 5238.

51 Z. Fan, D. Du, Z. Yu, P. Li, Y. Xia and J. Ouyang, *ACS Appl. Mater. Interfaces*, 2016, **8**, 23204.

52 C. a. Li, D. Luo, T. Wang, C. Shan, C. Li, K. Sun, A. K. K. Kyaw and J. Ouyang, *Small Struct.*, 2023, 2300245.

53 K. Jiang, S.-H. Hong, S.-H. Tung and C.-L. Liu, *J. Mater. Chem. A*, 2022, **10**, 18792.

54 R. Gusmao, Z. Sofer and M. Pumera, *Angew. Chem., Int. Ed.*, 2017, **56**, 8052.

55 J. Pang, A. Bachmatiuk, Y. Yin, B. Trzebicka, L. Zhao, L. Fu, R. G. Mendes, T. Gemming, Z. Liu and M. H. Rummeli, *Adv. Energy Mater.*, 2018, **8**, 1702093.

56 Y. Zhang, Y. Zheng, K. Rui, H. H. Hng, K. Hippalgaonkar, J. Xu, W. Sun, J. Zhu, Q. Yan and W. Huang, *Small*, 2017, **13**, 1700661.

57 Y. Xu, Z. Shi, X. Shi, K. Zhang and H. Zhang, *Nanoscale*, 2019, **11**, 14491.

58 J. Shao, H. Xie, H. Huang, Z. Li, Z. Sun, Y. Xu, Q. Xiao, X. F. Yu, Y. Zhao, H. Zhang, H. Wang and P. K. Chu, *Nat. Commun.*, 2016, **7**, 12967.

59 X. Zeng, M. Luo, G. Liu, X. Wang, W. Tao, Y. Lin, X. Ji, L. Nie and L. Mei, *Adv. Sci.*, 2018, **5**, 1800510.

60 T. G. Novak, H. Shin, J. Kim, K. Kim, A. Azam, C. V. Nguyen, S. H. Park, J. Y. Song and S. Jeon, *ACS Appl. Mater. Interfaces*, 2018, **10**, 17957.

61 W. Ou, B. Zhou, J. Shen, C. Zhao, Y. Y. Li and J. Lu, *iScience*, 2021, **24**, 101982.

62 A. Ozawa, M. Yamamoto, T. Tanabe, S. Hosokawa and T. Yoshida, *J. Mater. Chem. A*, 2020, **8**, 7368.

63 M. Liang, M. Zhang, S. Yu, Q. Wu, K. Ma, Y. Chen, X. Liu, C. Li and F. Wang, *Small*, 2020, **16**, 1905938.

64 Y. Wang, M. He, S. Ma, C. Yang, M. Yu, G. Yin and P. Zuo, *J. Phys. Chem. Lett.*, 2020, **11**, 2708.

65 X. Guan and J. Ouyang, *CCS Chem.*, 2021, **3**, 2415.

66 D. K. Ko, Y. Kang and C. B. Murray, *Nano Lett.*, 2011, **11**, 2841.

67 J.-Y. Lee and Y.-J. Lin, *Synth. Met.*, 2016, **212**, 180.

68 H. Song and K. Cai, *Energy*, 2017, **125**, 519.

69 X. Huang, L. Deng, F. Liu, Z. Liu and G. Chen, *Chem. Eng. J.*, 2021, **417**, 129230.

70 X. Huang, L. Deng, F. Liu, Q. Zhang and G. Chen, *Energy Mater. Adv.*, 2021, **2021**, 1572537.

71 Y.-T. Lin, C.-Y. Lee, C.-Y. Wu, J.-M. Lin, T.-C. Lee, S.-H. Tung and C.-L. Liu, *J. Power Sources*, 2023, **556**, 232516.

72 L. Deng and G. Chen, *Nano Energy*, 2021, **80**, 105448.

73 M. h. Mohammadi, M. Eskandari and D. Fathi, *J. Alloys Compd.*, 2021, **877**, 160177.

74 A. Kumar, T. Dixit, I. A. Palani, D. Nakamura, M. Higashihata and V. Singh, *Phys. E*, 2017, **93**, 97.

75 X. Zhang, T. T. Li, H. T. Ren, H. K. Peng, B. C. Shiu, Y. Wang, C. W. Lou and J. H. Lin, *ACS Appl. Mater. Interfaces*, 2020, **12**, 55072.

76 X. Zhang, B. C. Shiu, T.-T. Li, X. Liu, H.-T. Ren, Y. Wang, C.-W. Lou and J.-H. Lin, *Chem. Eng. J.*, 2021, **426**, 131923.

77 X. Zhang, B. C. Shiu, T.-T. Li, X. Liu, H.-T. Ren, Y. Wang, C.-W. Lou and J.-H. Lin, *Sol. Energy Mater. Sol. Cells*, 2021, **232**, 111353.